Flexible near-infrared diffuse optical tomography with varied weighting functions of edge-preserving regularization

Liang-Yu Chen,[1] Min-Cheng Pan,[2,*] and Min-Chun Pan[1,3]

[1]Department of Mechanical Engineering, National Central University, Taoyuan County 320, Taiwan

[2]Department of Electronic Engineering, Tungnan University, New Taipei City 222, Taiwan

[3]Graduate Institute of Biomedical Engineering, National Central University, Taoyuan County 320, Taiwan

*Corresponding author: m2pan@mail.tnu.edu.tw

Received 11 September 2012; revised 17 December 2012; accepted 9 January 2013;
posted 10 January 2013 (Doc. ID 176015); published 13 February 2013

In this paper, a flexible edge-preserving regularization algorithm based on the finite element method is proposed to reconstruct the optical-property images of near-infrared diffuse optical tomography. This regularization algorithm can easily incorporate with varied weighting functions, such as a generalized Lorentzian function, an exponential function, or a generalized total variation function. To evaluate the performance, results obtained from Tikhonov or edge-preserving regularization are compared with each other. As found, the edge-preserving regularization with the generalized Lorentzian function is more attractive than that with other functions for the estimation of absorption-coefficient images concerning functional tomographic images to discover functional information of tested phantoms/tissues. © 2013 Optical Society of America

OCIS codes: 100.3190, 170.3010, 170.6960.

1. Introduction

Advances have been made rapidly in various imaging modalities of optical tomography since computed tomography (CT) apparatus was first introduced in the 1970s and related modalities were investigated [1]. Meanwhile, diffuse optical tomography (DOT) providing functional information related to tissues has drawn great attention for the last two decades. However, near-infrared diffuse optical tomography (NIR DOT) imaging techniques suffer from low spatial-frequency resolution owing to the diffusive nature of scattered light. To solve this drawback, it can be coped with by the help of various reconstruction methods of NIR DOT. To understand the related information, readers can refer that the theory of NIR DOT was thoroughly reviewed [2] as well as edge-preserving regularization applied in computed imaging was first proposed and investigated in detail [3].

Some researchers have reported how to design a weighting function or use multiple weighting functions for processing images. A hybrid model was proposed for variational image restoration using an alternative diffusion switching a nonquadratic function with a parameter so as to preserve edges [4]. Based on potential functions with an adaptive rest condition, a regularization formulation was introduced for inverse problems in computer vision [5]. By considering particular families of dyadic wavelets, new potential functions were used, thereby preserving and restoring important image features, such as edges and smooth regions [6]. A deterministic relaxation algorithm was generalized and introduced for edge-preserving regularization in linear inverse problems [7]. A decomposition-enabled edge-preserving image restoration algorithm was proposed for

1559-128X/13/061173-10$15.00/0

maximizing the likelihood function [8]. To improve the performance and the convergence speed, an inversion method was developed by constructing a new objective function with edge-preserving regularization and a soft constraint [9,10]. An iterative split-gradient method was applied to confocal microscopy for investigating the effect of several edge-preserving priors, which was found stable, robust, and tolerant at various Poisson noise levels [11].

In addition, choosing an appropriate regularization parameter is essential for processing. A model of estimating the parameter was established to balance a data fidelity term and a regularization term in the objective function with a corresponding value to each one of some blocks in an image [12]. A constrained optimization approach was studied for the removal of Poisson noise [13]. For satellite image restoration, an edge-preserving regularization model was applied with a function φ involving two hyperparameters estimated by a Markov chain Monte Carlo maximum-likelihood technique [14].

Furthermore, edge-preserving regularization has been performed on the following aspects. With edge-preserving potential functions based on using a conjugate gradient method, a regularization scheme was proposed for the reconstruction of the complex permittivity profile [15]. An edge-preserving and quadratic regularization function was presented to solve a Poisson distribution of data-noise problem [16] and an edge-preserving regularization technique was used to estimate the discontinuities and decrease the sensitivity to noise during the reconstruction process of the microwave inverse problem [17]. Half-quadratic edge-preserving image restoration method was proposed to enhance CT images [18]. A three-dimensional regularization method was proposed for positron emission tomography transmission reconstruction where the objective function incorporates nonlocal boundary information, thereby minimizing its space-variant quadratic objective function to update the image estimate [19]. Coupled with an edge-preserving regularization process, a variational model was used for image classification [20]. Based on half-quadratic regularization and complementary *a priori* information, an edge-preserving regularization method was applied to magnetic induction tomography [21]. An edge-preserving deterministic regularization was presented for image restoration by minimizing the nonquadratic criterion [22].

Therefore, it can be seen that most edge-preserving regularization methods were applied to image restoration or some medical imaging systems rather than the NIR DOT imaging system. To the best of our knowledge, we first employed the edge-preserving regularization in NIR DOT [23]; subsequently, the comparison is made between Tikhonov and edge-preserving regularization with various weighting functions in this paper. Thus, there are two algorithms, Tikhonov and edge-preserving regularization; the former is a standard method and the latter is flexible as it can easily incorporate with varied weighting functions. The reason of the edge-preserving regularization applied to NIR DOT is that its advantage is able to create the edge enhancement of the reconstructed images with the edge-like information from the measured signals for image reconstruction. Our previous research has mainly discussed the methodology of edge-preserving regularization on NIR DOT; in addition, there remain some issues to be investigated. Therefore, this paper aims at further exploring the edge-preserving regularization algorithm in NIR DOT by comparing several regularization weighting functions; as a result, an appropriate weighting function for use is suggested.

2. Ring-Scanning-Based Imaging System

This section describes the ring-scanning-based imaging system including the image reconstruction algorithm of edge-preserving regularization with varied regularization weighting functions, a developed ring-based scanning device, and an optoelectronic measurement module.

A. Reconstruction Algorithm

An image reconstruction task contains forward modeling and inverse problem. The forward computation consists in obtaining the photon fluence rate out of a subject under investigation for a given source, and the initial-guess (or iterated result) on scattering and absorption coefficients. The inverse computation is to compute the scattering and absorption coefficients for a known light source and measured photon fluence rate in an iterative manner.

Such a physical process of NIR light illuminating through a highly-scattering medium can be approximated by the diffusion equation,

$$\nabla \cdot \kappa(\mathbf{r}) \nabla \Phi(\mathbf{r}, \omega) - \left[\mu_a(\mathbf{r}) - \frac{i\omega}{c} \right] \Phi(\mathbf{r}, \omega) = -S(\mathbf{r}, \omega), \tag{1}$$

where $\Phi(\mathbf{r}, \omega)$ is the photon fluence rate at position $\mathbf{r}$ and ω is the light intensity-modulation frequency, $S(\mathbf{r}, \omega)$ is the isotropic source term and c is the speed of light in tissue, as well as μ_a and κ denote the optical absorption and diffusion coefficients, respectively. For solving Eq. (1), numerical computation based on the finite element method derived by the Galerkin weak form of Eq. (1) using a boundary condition, $-\kappa \nabla \Phi \cdot \hat{n} = \alpha \Phi$ (flux in fact), can be implemented, where the solution $\Phi(\mathbf{r}, \omega)$ is approximated by the piecewise function ϕ_j at N vertex nodes over the problem domain Ω, $\Phi = \sum_{j=1}^{N} \Phi_j \phi_j(\mathbf{r})$. Thus, the following equation in a matrix form can be obtained:

$$\mathbf{A}\Phi = \mathbf{C}, \tag{2}$$

where

$$\mathbf{A}_{ij} = \int_{\Omega} -\kappa(\mathbf{r})\nabla\phi_i(\mathbf{r})\cdot\nabla\phi_j(\mathbf{r}) - \left[\mu_a(\mathbf{r}) - \frac{i\omega}{c}\right]\phi_i(\mathbf{r})\phi_j(\mathbf{r})d\mathbf{r} + \alpha\int_{\partial\Omega}\phi_i(\mathbf{r})\phi_j(\mathbf{r})d\mathbf{r},$$
$$\mathbf{C}_i = \int_{\Omega} -S(\mathbf{r},\omega)\phi_i(\mathbf{r})d\mathbf{r}. \quad (3)$$

More details in derivation can be found in [2]. Obviously, the forward solution, Φ, can be evaluated through Eq. (2). In terms of the physical process, the fluence rate matrix Φ is quantitatively and qualitatively dependent upon the source matrix $\mathbf{C}$ and the optical-property matrix $\mathbf{A}$, respectively, where the optical-property matrix $\mathbf{A}$ is the inertia of the material in spite of relating to the wavelength. Partially differentiating Eq. (2) with $\partial/\partial\mu_a$ and $\partial/\partial\kappa$, respectively, yields

$$\frac{\partial\Phi}{\partial\boldsymbol{\mu}_a} = -\mathbf{A}^{-1}\frac{\partial\mathbf{A}}{\partial\boldsymbol{\mu}_a}\Phi + \mathbf{A}^{-1}\frac{\partial\mathbf{C}}{\partial\boldsymbol{\mu}_a}$$
$$\frac{\partial\Phi}{\partial\boldsymbol{\kappa}} = -\mathbf{A}^{-1}\frac{\partial\mathbf{A}}{\partial\boldsymbol{\kappa}}\Phi + \mathbf{A}^{-1}\frac{\partial\mathbf{C}}{\partial\boldsymbol{\kappa}}. \quad (4)$$

With an approximation to applying the Taylor expansion method and ignoring higher-order terms, we obtain

$$\mathbf{J}\Delta\boldsymbol{\chi} = \Delta\Phi, \quad (5)$$

where the Jacobian matrix $\mathbf{J}$ denotes the matrix consisting of $\partial\Phi/\partial\boldsymbol{\mu}_a$ and $\partial\Phi/\partial\boldsymbol{\kappa}$, $\Delta\boldsymbol{\chi}$ is the vector composed of $\Delta\mu_a$ and $\Delta\kappa$, and $\Delta\Phi$ is the vector with differences between calculated photon fluence rate ($\Phi^{\text{cal.}}$) and measured photon fluence rate ($\Phi^{\text{meas.}}$). Then the elements of the Jacobian matrix can be calculated from Eq. (4).

In an edge-preserving regularization algorithm, the objective function is composed of a residual term and a regularization term where a potential function with edge-preserving properties is introduced into the regularized term. It is desirable to be able to incorporate varied weighting functions into the regularization term to achieve a high-quality result of NIR DOT. Along with the help of half-quadratic regularization to simplify the problem of nonlinearity shown in the original proposed objective function, the transformed objective function for NIR DOT can then be written [3,23] as Eq. (6),

$$Q^*_{\text{Ep}}(\Delta\boldsymbol{\chi},\mathbf{b}) = \|\mathbf{J}\Delta\boldsymbol{\chi} - \Delta\Phi\|_2^2 + \lambda^2\sum_l\sum_k\{(\mathbf{b}_l)_k(\mathbf{D}_l\Delta\boldsymbol{\chi})_k^2 + \varphi[(\mathbf{b}_l)_k]\}, \quad (6)$$

where the auxiliary variable $\mathbf{b} = (\mathbf{b}_1, \mathbf{b}_2, \ldots, \mathbf{b}_l, \ldots)$ is introduced by half-quadratic regularization and capable of making Eq. (6) linear in $\Delta\boldsymbol{\chi}$ when performing a minimization task, and φ originally determines the regularization imposed on every value of the first-order difference $\mathbf{D}_l\Delta\boldsymbol{\chi}$, which is used to detect the discontinuities of the update vector $\Delta\boldsymbol{\chi}$ in a specific direction l. In the subsequent minimization procedure, $\Delta\boldsymbol{\chi}^n$ is fixed at iteration step $n+1$ and $\mathbf{b}^{n+1}$ is computed using the following expression derived from the theorem proved in [3], i.e.,

$$(\mathbf{b}_l^{n+1})_k = \underset{(\mathbf{b}_l)_k}{\text{argmin}}\{Q^*_{\text{Ep}}(\Delta\boldsymbol{\chi}^n,(\mathbf{b}_l)_k)\} = \frac{\varphi'[(\mathbf{D}_l\Delta\boldsymbol{\chi}^n)_k]}{2(\mathbf{D}_l\Delta\boldsymbol{\chi}^n)_k}. \quad (7)$$

Then the new update vector $\Delta\boldsymbol{\chi}^{n+1}$ is obtained from the minimization of $Q^*_{Ep}(\Delta\boldsymbol{\chi},\mathbf{b}^{n+1})$ such that

$$\Delta\boldsymbol{\chi}^{n+1} = \underset{\Delta\boldsymbol{\chi}}{\text{argmin}}\{Q^*_{\text{Ep}}(\Delta\boldsymbol{\chi},\mathbf{b}^{n+1})\} = [\mathbf{J}^T\mathbf{J} + \lambda^2\Delta^{n+1}_{\text{Ep}}]^{-1}\mathbf{J}^T\Delta\Phi, \quad (8)$$

where $\Delta^{n+1}_{\text{Ep}} = \sum_l\mathbf{D}_l^T\mathbf{B}_l^{n+1}\mathbf{D}_l$ and $\mathbf{B}_l^{n+1} = \text{diag}[(\mathbf{b}_l^{n+1})_k]$. The optical parameters are predicted iteratively with using the update equations, i.e., Eqs. (7) and (8), alternately until the stopping criteria are met.

B. Varied Regularization Weighting Functions

To investigate the effect of the edge-preserving weighting function for NIR DOT, we employed varied functions for $\varphi'(t)/2t$ in Eq. (7). Teboul *et al.* [24] had summarized some commonly used edge-preserving weighting functions. By investigating those commonly used weighting functions, three functions were generalized and adopted in this study: a generalized Lorentzian (GL) function $(\gamma^2)^m/(\gamma^2+t^2)^m$, an exponential (EXP) function e^{-t^2}, and a generalized total variation (GTV) function $(\alpha/2)t^{\alpha-2}$. Hence, three weighting functions were separately used in both simulation and experimental data.

C. Ring-Based Scanning Device and Optoelectronic Measurement Module

In addition to the reconstruction algorithm of edge-preserving regularization, a ring-scanning-based measurement system of NIR DOT was constructed by using a single source and a detector that can separately rotate around the circumference of a tested phantom with a high degree of spatial flexibility. Furthermore, the optoelectronic measurement module was operated in the frequency domain to acquire the attenuated intensity and delayed phase of diffuse NIR light. The architecture of this frequency domain measurement module is shown in Fig. 1.

First of all, DC power supply provides a static voltage modulated with f MHz (up to 100 MHz) from channel one (CH1) of a function generator by coupling with a bias Tee, thereby leading a laser diode

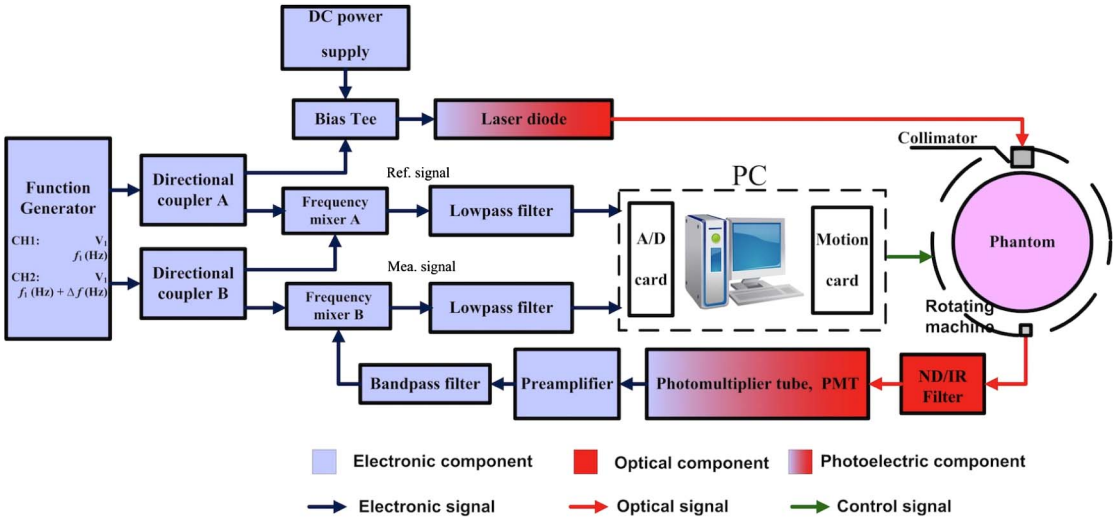

Fig. 1. (Color online) Architecture of the frequency domain optoelectronic measurement module associated with a ring-based scanning device.

to output an oscillating NIR light (830 nm) power. Subsequently, NIR light is transmitted to an optical fiber for each source position chosen with a motor of predefined parameters. Then, the source light passes through the tested phantom and the diffuse light emitted from the phantom at each detection is acquired with a liquid light guide to a photomultiplier tube (PMT); prior to the PMT, the diffuse light passes through an adaptive neutral density filter and an infrared filter in order to attenuate optical power and filter out other wavelengths, respectively. With a mixer, the measured signal is mixing with the other signal $f + \Delta f$ MHz from channel two (CH2) of the function generator; following that, the amplitude and phase of the measured signal are extracted in the low-frequency region with a low-pass filter. Similarly, a low-frequency referenced signal of amplitude and phase is obtained by mixing original signals (f MHz and $f + \Delta f$ MHz) with another pair of a mixer and a low-pass filter. Finally, the measured and the reference signals are acquired and recorded with a data acquisition board, thereby separately obtaining amplitude and phase information of the measured and the reference light. For acquiring experimental data, this measurement module was built with a single rotating source by a detector and can be operated at up to 100 MHz; measurements were recorded at 15 detections for a single source position and repeated in succession until data from 16 equivalent source positions, which yielded a total of 16×15 separate amplitude-attenuation and phase-delay observations for each image reconstruction.

3. Results and Discussion

In this section, the proposed flexible edge-preserving reconstruction algorithm is evaluated for varied weighting functions. An inhouse-coded reconstruction program named as NIR.FD_PC and a ring-based scanning measuring device operated on the frequency domain were implemented in the laboratory.

A. Evaluation Method

To obtain further quantitative information about the reconstructed images in these simulations, two measures [25] (contrast resolution and size resolution) were used over the region of interest. To define the contrast and size resolution in the one-dimensional (1D) and two-dimensional (2D) domains, the idea originates from precision and density/saturation, respectively, of which the advantage is easy to be implemented. The contrast resolution $R_{\text{cont.}}^{1D,2D}$ is defined to evaluate the resolution on the contrast of optical property values of the inclusion relative to the background, shown as

$$R_{\text{contrast}}^{1D,2D} = \frac{\left(\overline{\max}^{\text{inclusion}}/\overline{\min}^{\text{background}}\right)_{\text{reconstruction}}}{\left(\overline{\max}^{\text{inclusion}}/\overline{\min}^{\text{background}}\right)_{\text{Exact}}} \quad (9)$$

and

$$R_{\text{contrast}}^{1D,2D} = 2 - R_{\text{contrast}}^{1D,2D}, \quad \text{if } 1 < R_{\text{contrast}}^{1D,2D} < 2,$$

where $\overline{\max}$ and $\overline{\min}$ denote the average of maxima and minima over all the selected inclusion or background regions, respectively. The size resolution is designed to evaluate the resolution on the size over all inclusions as below:

$$R_{\text{size}}^{1D,2D} = \left\{\left[1 - \frac{(\text{MSE}^{\text{inclusion}})_{\text{Recon.2.Exact}}}{(\text{MSE}^{\text{inclusion}})_{\text{Exact.2.baseline}}}\right] R_{\text{contrast}}^{1D,2D}\right\}^{1/2}, \quad (10)$$

where mean square error (MSE) is calculated over the selected inclusion region between the exact value of the inclusion and the reconstruction or baseline value and a baseline value is used with the same as the background optical coefficients. It is noted that the size resolution in Eq. (10) includes the contrast resolution in order to prevent from size overestimation.

B. Numerical Simulation

In the simulation, we considered some practical situations. The simulated phantom has an 80 mm diameter background ($\mu_a = 0.006$ mm^{-1} and $\mu_s' = 0.6$ mm^{-1}) with a 10 mm diameter inclusion at a 15 mm off-center along the 45° axis, which has an absorption contrast of 2.5 : 1 and a scattering contrast of 1.4 : 1 level between the inclusion and the background. Of much more importance is how the weighting functions behave in the presence of uniformly distributed random variation in the phantom where the absorption and the reduced scattering coefficients (μ_a and μ_s') are ranging up to a ±80% variation relative to the mean value of background or inclusion. The modulation frequency was selected to be 20 MHz. For all the reconstruction cases shown in this study, the finite-element mesh consisting of 4225 nodes and 8192 triangle elements was used to generate simulated data and a second mesh consisting of 871 nodes and 1536 triangle elements was adopted in the reconstruction procedure [23]. Moreover, no more than 30 iteration steps were used and each iteration step took computation time about 10 s.

Figure 2 presents image reconstructions of the simulated phantom having no variation, obtained from varied weighting functions. Considerable improvement can be observed in the reconstructed images when Lorentzian, exponential, or total variation function is invoked compared with Tikhonov regularization where much more ringing artifact was, however, produced in the absorption or reduced scattering image for reconstruction using exponential or total variation function. In edge-preserving regularization, the weighting function satisfies the condition that it is strictly decreasing, i.e., an edge, featuring with a large gradient value, is preserved by assigning a small weight value [3]. Therefore, in order to minimize the ringing artifacts when using edge-preserving regularization, one can appropriately choose the decreasing rate of the weighting function. In terms of this, the generalized Lorentzian weighting function proposed in this study appears to have more suitable decreasing rate compared with exponential and generalized total variation weighting functions. To provide a more quantitative assessment of these images, Fig. 3 corresponding to Fig. 2 is included, in which the reconstructed optical-property distributions compared with the exact value are displayed along a 1D circular profile through the center of the inclusion region. The comparative improvement of the absorption or the reduced scattering image is apparent for varied weighting functions.

To simulate the variations of optical coefficients in the breast, other cases have been performed and investigated for the edge-preserving regularization respectively incorporated with varied weighting functions under the condition of uniformly distributed variation of 20%, 40%, 60%, and 80% in exact optical coefficient distribution μ^{exact}. Those uniformly distributed random variations were added over the whole imaging domain; the varied optical coefficient distribution μ^{varied} is generated by the formula $\mu^{\text{varied}} = \mu^{\text{exact}} + p \times \mu^{\text{exact}} \times n$, where n is uniformly distributed random number between $[-1, 1]$, and p is set to be 20%, 40%, 60%, and 80% in this study. As found in the simulation, the improvement of the reconstructions by the incorporation of the weighting function is obvious over that achieved with Tikhonov regularization; it is shown that even in the presence of strong random variation the proposed algorithm is still able to recover the main features of the phantom.

As can be seen in Table 1 or Fig. 4, the edge-preserving regularization with the generalized Lorentzian function exhibits a quality near true value of optical property especially in absorption rather

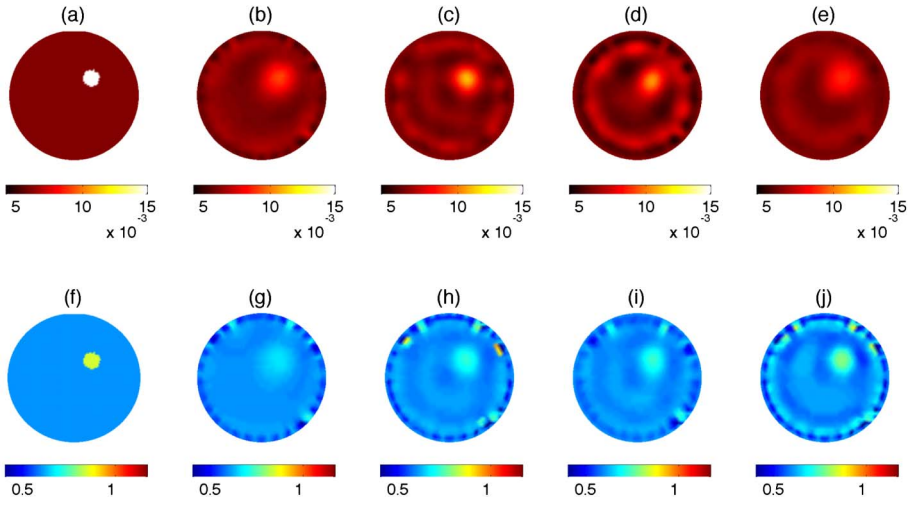

Fig. 2. (Color online) Demonstration of reconstructed absorption and reduced scattering images of a breast-like phantom from simulated data: (a) designated distribution of absorption coefficient with no variation and the reconstructed absorption images using (b) Tikhonov, (c) generalized Lorentzian function, (d) exponential function, and (e) generalized total variation function as well as (f) designated distribution of reduced scattering coefficient with no variation and the reconstructed reduced scattering images using (g) Tikhonov, (h) generalized Lorentzian function, (i) exponential function, and (j) generalized total variation function.

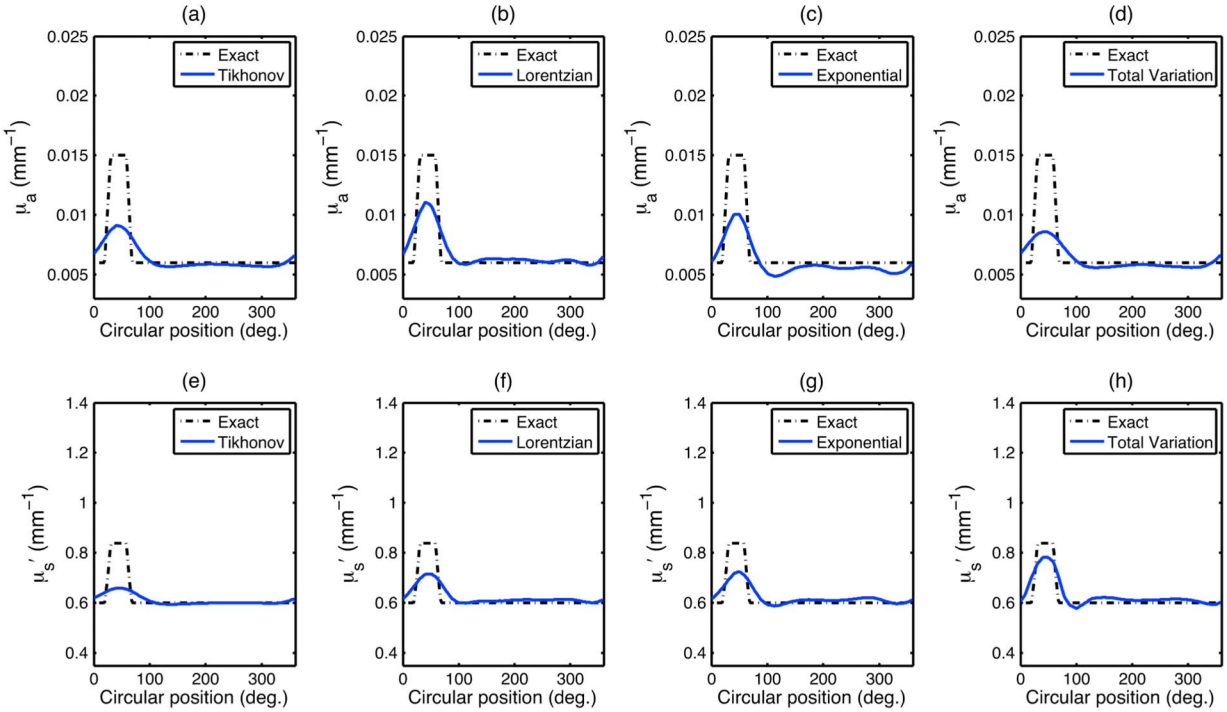

Fig. 3. (Color online) 1D circular profiles corresponding to Fig. 2.

than other approaches, and that with the generalized total variation function shows a better-quality reconstruction in the reduced scattering property.

C. Experimental Trials

Our proposed regularization method with different weighting functions was also justified using experimental data under the conditions of both measurement noise and slight optical coefficients variation in the phantom. A 50 mm diameter cylindrical phantom was made for the reconstructions using experimental data, of which the $\mu_a = 0.006$ mm^{-1} and $\mu_s' = 0.6$ mm^{-1} were composed of a fat emulsion suspension (Lipovenoes) as a scattering medium and ink

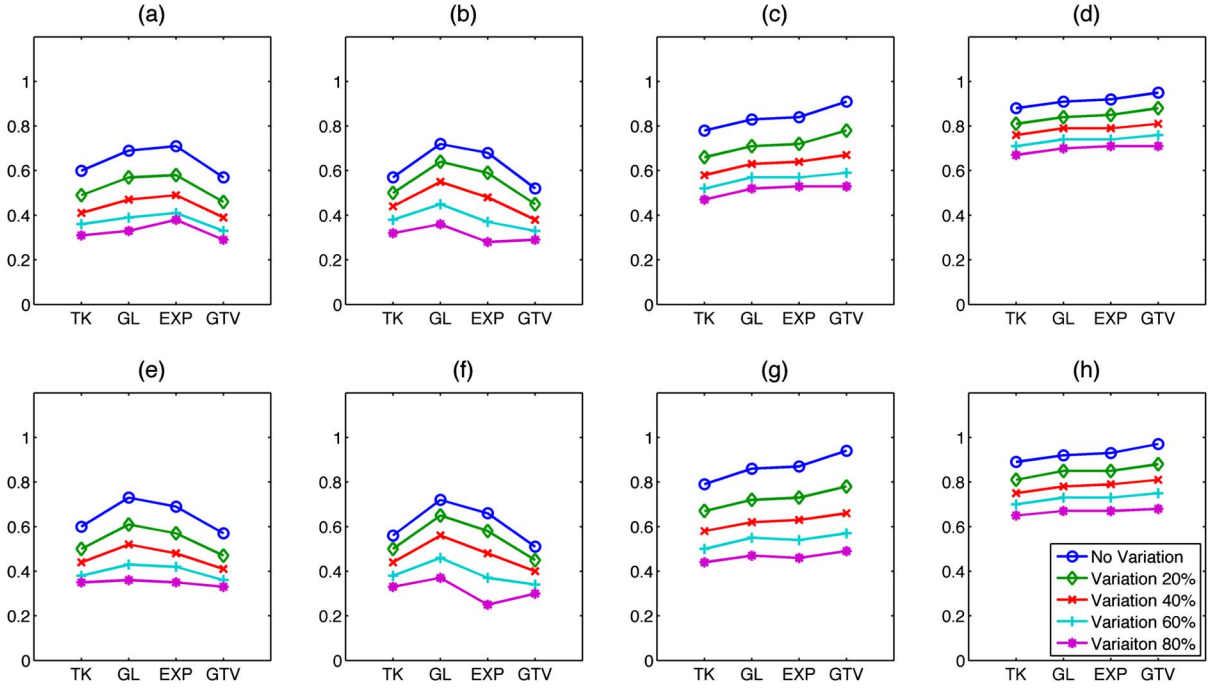

Fig. 4. (Color online) Comparison of contrast and size resolutions of simulation cases for Tikhonov and edge-preserving regularization corresponding to Table 1: 1D cases, (a) contrast resolution of μ_a, (b) size resolution of μ_a, (c) contrast resolution of μ_s', (d) size resolution of μ_s', and 2D cases, (e) contrast resolution of μ_a, (f) size resolution of μ_a, (g) contrast resolution of μ_s', (h) size resolution of μ_s'.

Table 1. Evaluation on Contrast and Size Resolutions of Simulation Cases for Tikhonov and Edge Preserving Regularization

	μ_a								μ_s'							
	TR		GL		EXP		GTV		TR		GL		EXP		GTV	
	Contrast	Size	Contrast	Size	Contrast	Size	Contrast	Size	Contrast	Size	Contrast	Size	Contrast	Size	Contrast	Size
1D																
Variation Free	0.58	0.56	0.66	0.71	0.68	0.67	0.56	0.52	0.77	0.88	0.82	0.90	0.83	0.91	0.89	0.94
Variation 20%	0.56	0.54	0.63	0.68	0.65	0.62	0.53	0.48	0.79	0.88	0.84	0.91	0.85	0.92	0.91	0.95
Variation 40%	0.54	0.50	0.60	0.62	0.62	0.54	0.51	0.44	0.81	0.89	0.87	0.92	0.87	0.93	0.92	0.95
Variation 60%	0.51	0.45	0.56	0.54	0.58	0.44	0.48	0.40	0.82	0.89	0.89	0.93	0.90	0.93	0.94	0.95
Variation 80%	0.49	0.40	0.52	0.45	0.54	0.33	0.46	0.36	0.84	0.89	0.91	0.93	0.91	0.93	0.95	0.95
Average	0.54	0.49	0.60	0.60	0.61	0.52	0.51	0.44	0.81	0.89	0.87	0.92	0.87	0.92	0.92	0.95
2D																
Variation Free	0.58	0.55	0.67	0.69	0.63	0.63	0.55	0.51	0.79	0.88	0.84	0.91	0.85	0.92	0.91	0.95
Variation 20%	0.57	0.54	0.67	0.68	0.62	0.60	0.54	0.49	0.83	0.91	0.88	0.94	0.89	0.94	0.96	0.98
Variation 40%	0.57	0.51	0.65	0.63	0.58	0.53	0.54	0.46	0.87	0.93	0.93	0.96	0.94	0.96	0.99	0.99
Variation 60%	0.57	0.47	0.63	0.55	0.53	0.42	0.53	0.42	0.92	0.94	0.98	0.98	0.97	0.97	0.97	0.98
Variation 80%	0.56	0.42	0.59	0.47	0.47	0.29	0.53	0.39	0.95	0.95	0.99	0.98	0.96	0.96	0.96	0.96
Average	0.57	0.50	0.64	0.60	0.56	0.49	0.54	0.45	0.87	0.92	0.93	0.95	0.92	0.95	0.96	0.97

added as an absorber. In the phantom, there was a 10 mm diameter inclusion with 4∶1 absorption and reduced scattering contrast and placed along 45°. Figure 5 displays the reconstructed optical-property images; 1D circular profiles of Fig. 5 are shown as Fig. 6 for a detailed comparison of the reconstructions. Similar to the reconstructions with simulated data, the results using the generalized Lorentzian and the generalized total variation are correspondingly superior for the characterization of absorption coefficients and reduced scattering coefficients. Note that the results using Tikhonov or an exponential weighting function seem well reconstructed in absorption images; actually, the absorption coefficients were overestimated. For further inspection, the reconstructed optical images of phantom targets presented in Fig. 5 have fewer artifacts in comparison with the reconstructed images of simulated data with no variation shown in Fig. 2. The reason is described as follows. Prior to applying the measured heterogeneous data $\Phi_{\text{hetero}}^{\text{measured}}$ for image reconstruction, we performed calibrations using the measured and computed homogeneous data, $\Phi_{\text{homo}}^{\text{measured}}$ and $\Phi_{\text{homo}}^{\text{computed}}$, respectively. The computed homogeneous data were obtained from a homogeneous phantom with assigned background optical-property coefficients. The calibration was carried out by applying the following calibration equation to the measured heterogeneous data:

$$\Phi_{\text{hetero}}^{\text{computed}} = \Phi_{\text{hetero}}^{\text{measured}} \frac{\Phi_{\text{homo}}^{\text{computed}}}{\Phi_{\text{homo}}^{\text{measured}}}. \tag{11}$$

This procedure estimates the unknown scaling and coupling coefficients between the measurement and computation, and thus the system-based offset

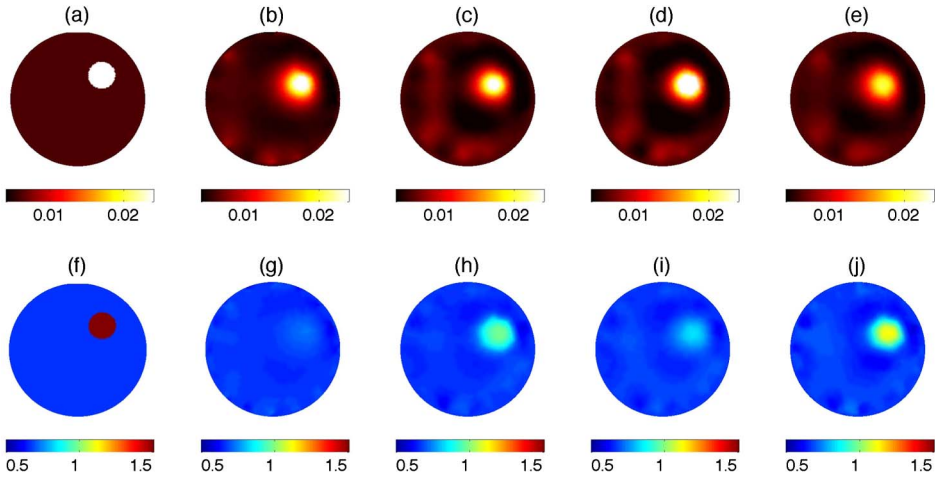

Fig. 5. (Color online) Demonstration of reconstructed absorption and reduced scattering images of a breast-like phantom from experimental data: (a) phantom with designated absorption properties and the reconstructed absorption images using (b) Tikhonov, (c) generalized Lorentzian function, (d) exponential function, and (e) generalized total variation function as well as (f) phantom with designated reduced scattering properties and the reconstructed reduced scattering images using (g) Tikhonov, (h) generalized Lorentzian function, (i) exponential function, and (j) generalized total variation function.

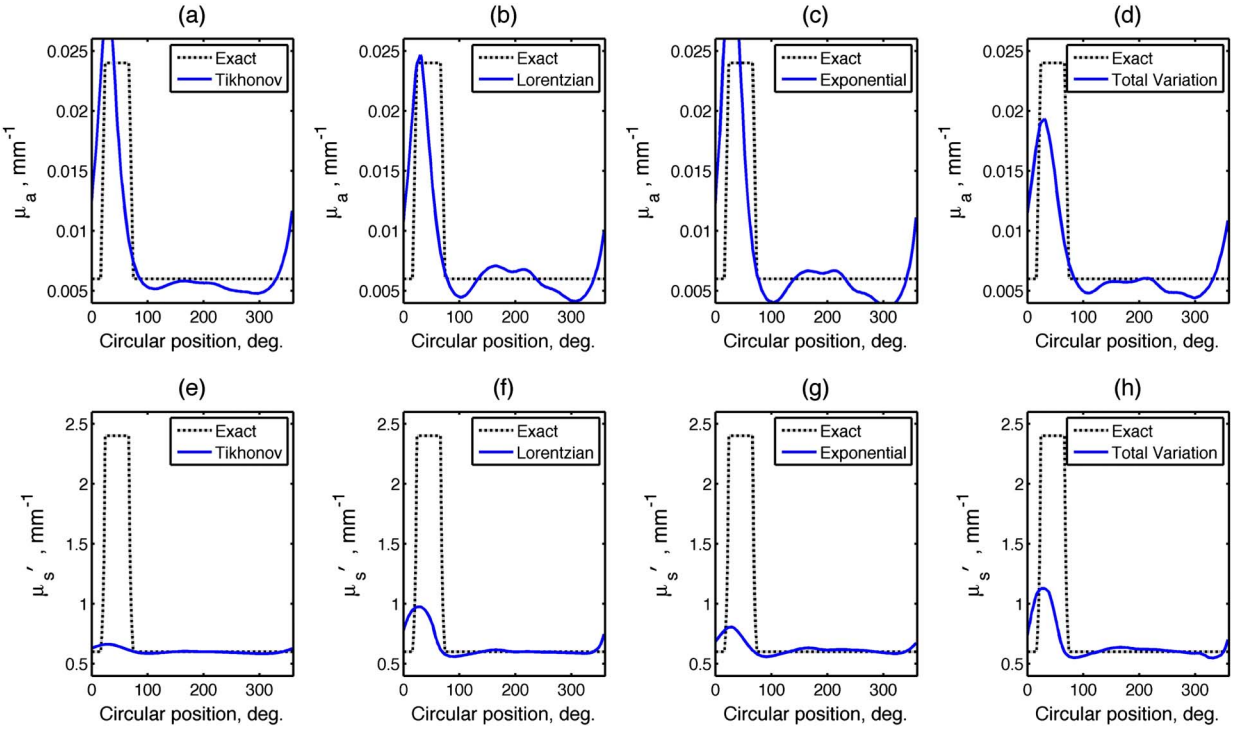

Fig. 6. (Color online) 1D circular profiles corresponding to Fig. 5.

resulting from measured data can be removed. Because of this calibration, the artifacts resulted in the reconstructed images from measured data can be significantly reduced as compared to those reconstructed from simulated data. In other words, artifacts in the simulation arise from the mismatch between forward and inverse meshes without further calibration.

As to simulate different cross sections of breast, the following experimental phantom with a diameter of 80 mm was studied. The phantom with two inclusions was imaged at different modulated lights of 20, 50, and 70 MHz. A Lipovenoes-and-ink solution was made for the phantom background with two 10 mm diameter and 3:1 absorption and reduced scattering contrast cylindrical rods placed

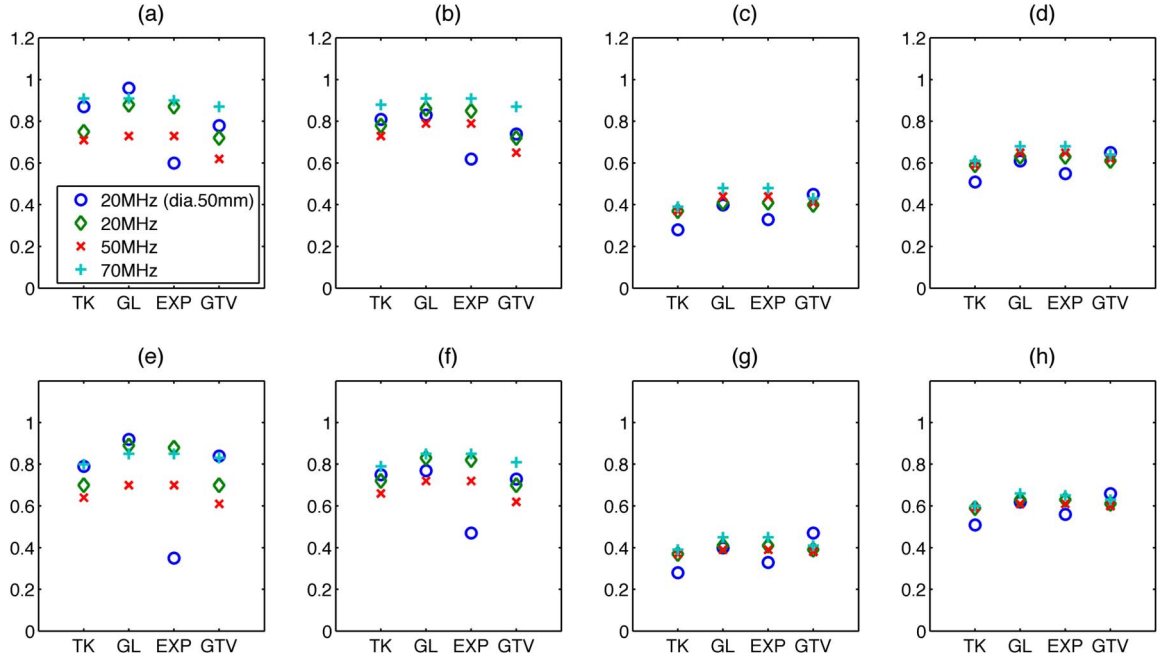

Fig. 7. (Color online) Comparison of contrast and size resolutions of experiment cases for Tikhonov and edge-preserving regularization corresponding to Table 2: 1D cases, (a) contrast resolution of μ_a, (b) size resolution of μ_a, (c) contrast resolution of μ_s', (d) size resolution of μ_s', and 2D cases, (e) contrast resolution of μ_a, (f) size resolution of μ_a, (g) contrast resolution of μ_s', (h) size resolution of μ_s'.

Table 2. Evaluation on Contrast and Size Resolutions of Experiment Cases for Tikhonov and Edge-Preserving Regularization

	μ_a								μ_s'							
	TR		GL		EXP		GTV		TR		GL		EXP		GTV	
	Contrast	Size	Contrast	Size	Contrast	Size	Contrast	Size	Contrast	Size	Contrast	Size	Contrast	Size	Contrast	Size
1D																
20 MHz (Phantom 50 mm)	0.87	0.81	0.96	0.83	0.60	0.62	0.78	0.74	0.28	0.51	0.40	0.61	0.33	0.55	0.45	0.65
20 MHz	0.75	0.78	0.88	0.86	0.87	0.85	0.72	0.72	0.37	0.59	0.41	0.63	0.41	0.63	0.40	0.61
50 MHz	0.71	0.73	0.73	0.79	0.73	0.79	0.62	0.65	0.37	0.59	0.44	0.65	0.44	0.65	0.41	0.62
70 MHz	0.91	0.88	0.91	0.91	0.90	0.91	0.87	0.87	0.39	0.61	0.48	0.68	0.48	0.68	0.43	0.64
Average	0.81	0.80	0.87	0.85	0.78	0.79	0.75	0.75	0.35	0.58	0.43	0.64	0.41	0.63	0.42	0.63
2D																
20 MHz (Phantom 50 mm)	0.79	0.75	0.92	0.77	0.35	0.47	0.84	0.73	0.28	0.51	0.40	0.62	0.33	0.56	0.47	0.66
20 MHz	0.70	0.72	0.89	0.83	0.88	0.82	0.70	0.70	0.37	0.59	0.41	0.63	0.41	0.63	0.39	0.61
50 MHz	0.64	0.66	0.70	0.72	0.70	0.72	0.61	0.62	0.37	0.59	0.39	0.61	0.39	0.61	0.38	0.60
70 MHz	0.80	0.79	0.85	0.85	0.85	0.85	0.83	0.81	0.39	0.60	0.45	0.66	0.45	0.65	0.41	0.63
Average	0.73	0.73	0.84	0.79	0.69	0.72	0.75	0.71	0.35	0.57	0.41	0.63	0.40	0.61	0.41	0.63

along $180° \pm 45°$ in the interior. Likewise, Table 2 and Fig. 7 show the quantitative evaluation of experimental examples. As shown, a same remark can be made; i.e., the edge-preserving regularization with the generalized Lorentzian function and the generalized total variation function demonstrate a superior estimation in the absorption and the reduced scattering property, respectively.

As can be seen in simulation cases (Table 1), the regularization with the generalized Lorentzian function for absorption-coefficient images basically possesses the highest average values up to 0.64 and 0.60 in contrast and size resolution, respectively, and the regularization with the generalized total variation function for reduced-scattering-coefficient images has the highest average values up to 0.96 and 0.97; for a similar comparison among experimental cases (Table 2), the former, 0.84 and 0.79, as well as the latter, 0.41 and 0.63. Even though the regularization with the generalized total variation function performs well in the reduced-scattering-coefficient images, the performance of the regularization with the generalized Lorentzian function is next to that with the generalized total variation function.

With the multiple wavelengths, as known, the concentrations of the three chromophores (oxyhemoglobin, deoxyhemoglobin, and water) can be estimated from absorption coefficients whereas the spectral character of the reduced scattering coefficient provides information about the structural composition of the tissue, which depend on scatter size and number density associated with age and radiographic density. Concerning functional tomographic images, it is suggested that using the edge-preserving regularization associated with the generalized Lorentzian function as a weighting function is the most attractive compared with other functions for the estimation of absorption-coefficient images from which functional information like oxyhemoglobin and deoxyhemoglobin concentration can be further characterized with a spectral prior.

4. Conclusion

The significance of this work is important for the field of NIR DOT. The advantages of the edge-preserving regularization with a weighting function penalizing the objective function are: (1) flexibility: a flexible framework to incorporate varied weighting functions as required, (2) easy implementation: the use of any weighting function is to simply replace $\varphi'(t)/2t$ in Eq. (7), and (3) effectiveness: the weighting function used is able to enhance the difference between the inclusion and background. As shown in previous sections, this framework enables us to impose an appropriate function for estimating images of the absorption and the reduced scattering coefficients, and to obtain a better-quality result rather than the optical properties derived from a rigid algorithm. Our aim is not to provide a rigorous comparison between these weighting functions, and in practice this would require more experiments, but to give some indications about their behavior. Even so, relative variation up to 80% was considered for numerical simulations as well as varied intensity-modulation lights and cross sections were tested for experiments; results show the proposed algorithm effective, i.e., the inclusions are not buried by optical-coefficient variation or because of low modulated frequency.

Furthermore, a perspective of this work is the quantitative comparison between the proposed edge-preserving and Tikhonov reconstruction algorithms in both terms of 1D and 2D in quality. As demonstrated, the improvement to images can be achieved when edge-preserving regularization is used for the optical-property reconstruction. Based on the view point of functional images, we suggest that an appropriate choice is to use the edge-preserving regularization with the generalized Lorentzian weighting function for optical-coefficient image reconstruction, of which the contrast and size resolution can be up to 0.84, 0.79 for absorption and 0.41, 0.63 for the reduced-scattering coefficient in experimental cases.

References

1. P. J. Cassidy and G. K. Radda, "Molecular imaging perspectives," J. R. Soc. Interface **2**, 133–144 (2005).
2. S. R. Arridge and J. C. Schotland, "Optical tomography: forward and inverse problems," Inverse Probl. **25**, 123010 (2009).
3. P. Charbonnier, L. Blanc-Feraud, G. Aubert, and M. Barlaud, "Deterministic edge-preserving regularization in computed imaging," IEEE Trans. Image Process. **6**, 298–311 (1997).
4. V. B. S. Prasath and A. Singh, "A hybrid convex variational model for image restoration," Appl. Math. Comput. **215**, 3655–3664 (2010).
5. M. Rivera and J. L. Marroquin, "Adaptive rest condition potentials: first and second order edge-preserving regularization," Comput. Vis. Image Underst. **88**, 76–93 (2002).
6. D. Lazzaro and L. B. Montefusco, "Edge-preserving wavelet thresholding for image denoising," J. Comput. Appl. Math. **210**, 222–231 (2007).
7. A. H. Delaney and Y. Bresler, "Globally convergent edge-preserving regularized reconstruction: an application to limited-angle tomography," IEEE Trans. Image Process. **7**, 204–221 (1998).
8. R. Pan and S. J. Reeves, "Efficient Huber-Markov edge-preserving image restoration," IEEE Trans. Image Process. **15**, 3728–3735 (2006).
9. H. Zhang, Z. Shang, and C. Yang, "A non-linear regularized constrained impedance inversion," Geophys. Prospect. **55**, 819–833 (2007).
10. H. Zhang, Z. Shang, and C. Yang, "Adaptive reconstruction method of impedance model with absolute and relative constraints," J. Appl. Geophys. **67**, 114–124 (2009).
11. G. Vicidomini, P. Boccacci, A. Diaspro, and M. Bertero, "Application of the split-gradient method to 3D image deconvolution in fluorescence microscopy," J. Microsc. **234**, 47–61 (2009).
12. X. Gu and L. Gao, "A new method for parameter estimation of edge-preserving regularization in image restoration," J. Comput. Appl. Math. **225**, 478–486 (2009).
13. R. Zanella, P. Boccacci, L. Zanni, and M. Bertero, "Efficient gradient projection methods for edge-preserving removal of Poisson noise," Inverse Probl. **25**, 045010 (2009).
14. A. Jalobeanu, L. Blance-Feraud, and J. Zerubia, "Hyperparameter estimation for satellite image restoration using a MCMC maximum-likelihood method," Pattern Recogn. **35**, 341–352 (2002).
15. P. Lobel, L. Blanc-Feraud, Ch. Pichot, and M. Barlaud, "A new regularization scheme for inverse scattering," Inverse Probl. **13**, 403–410 (1997).
16. J. M. Bardsley and J. Goldes, "An iterative method for edge-preserving MAP estimation when data-noise is Poisson," SIAM J. Sci. Comput. **32**, 171–185 (2010).
17. B. Omrane, Y. Goussard, and J. Laurin, "Constrained inverse near-field scattering using high resolution wire grid models," IEEE Trans. Antennas Propag. **59**, 3710–3718 (2011).
18. N. Villain, Y. Goussard, J. Idier, and M. Allain, "Three-dimensional edge-preserving image enhancement for computed tomography," IEEE Trans. Med. Imag. **22**, 1275–1287 (2003).
19. D. F. Yu and J. A. Fessler, "Three-dimensional non-local edge-preserving regularization for PET transmission reconstruction," in *Nuclear Science Symposium Conference Record* (IEEE, 2000), pp. 1566–1570.
20. C. Samson, L. Blanc-Feraud, G. Aubert, and J. Zerubia, "A variational model for image classification and restoration," IEEE Trans. Pattern Anal. Mach. Intell. **22**, 460–472 (2000).
21. R. Casanova, A. Silva, and A. R. Borges, "MIT image reconstruction based on edge-preserving regularization," Physiol. Meas. **25**, 195–207 (2004).
22. L. Blanc-Feraud and M. Barlaud, "Edge preserving restoration of astrophysical images," Vistas Astron. **40**, 531–538 (1996).
23. L. Y. Chen, M.-C. Pan, and M.-C. Pan, "Implementation of edge-preserving regularization for frequency-domain diffuse optical tomography," Appl. Opt. **51**, 43–54 (2012).
24. S. Teboul, L. Blanc-Feraud, G. Aubert, and M. Barlaud, "Variational approach for edge-preserving regularization using coupled PDE's," IEEE Trans. Image Process. **7**, 387–397 (1998).
25. M.-C. Pan, C. H. Chen, L. Y. Chen, M.-C. Pan, and Y. M. Shyr, "Highly resolved diffuse optical tomography: a systematic approach using high-pass filtering for value-preserved images," J. Biomed. Opt. **13**, 024022 (2008).